

# Blur Compensation Weighted Calibration Algorithm for Stereo Vision

Yong-Chang Li\* and Jing Jiang

Beijing Union University, Beijing, 100101 China

{20221081210212, xxtjiangjing}@buu.edu.cn

Received 9 January 2025; Revised 10 May 2025; Accepted 5 July 2025

**Abstract.** The focus settings and physical characteristics of lenses significantly affect distortion correction, particularly under blurred imaging conditions, thereby limiting the measurement accuracy of existing stereo vision systems. Moreover, traditional calibration processes for stereo vision systems are complex due to the need for precise focus distance adjustments and careful calibration board selection. In this paper, we propose a camera parametric model based on weighted radial constraints that accounts for both radial and non-central lens distortion. This model aims to improve calibration accuracy while simplifying the calibration workflow. Additionally, we introduce a stereo vision correction method that utilizes speckle patterns as calibration images and eliminates the requirement for precise camera focusing. This approach is more user-friendly than conventional planar chessboard techniques, as it avoids frequent lens adjustments for optimal focus. Experimental results demonstrate improvements in accuracy of 17.2% and 15.6% over Zhang's and Tsai's calibration methods, respectively.

**Keywords:** camera calibration, distortion model, stereo vision

## 1 Introduction

In modern three-dimensional measurement systems, such as those used in autonomous driving [1-3], industrial inspection [4-6], and robotic navigation [7-9], camera calibration accuracy directly impacts system performance. Representative application scenarios of stereo calibration are illustrated in Fig. 1. Traditional calibration methods, such as Zhang's planar calibration [10], typically rely on ideal lens models, precise focusing, and high-quality calibration targets. However, real-world conditions often diverge substantially from these assumptions, necessitating reliable calibration methods for industrial cameras.

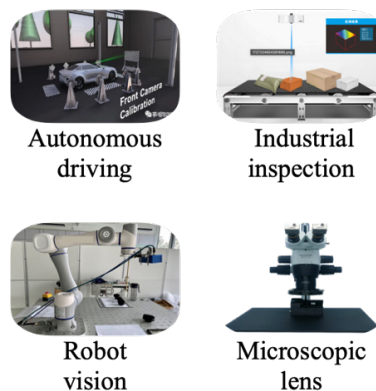


Fig. 1. Representative scenes for stereo camera calibration

Standard stereo calibration procedures usually require the calibration target to occupy approximately 70% of the camera's field of view to achieve optimal results. However, operational environments may constrain the cal-

\* Corresponding Author

ibration distance, leading to discrepancies between the actual working depth and the intended calibration depth. For example, in scenarios involving fast-moving robotic arms, captured images often exhibit significant out-of-focus blur due to motion [11], complicating accurate feature extraction and calibration.

Zhang’s calibration method assumes an idealized pinhole camera model, which neglects complex distortions and out-of-focus effects commonly encountered in practice. These limitations—arising from lens manufacturing defects, alignment errors, and blur—reduce the accuracy of calibration and subsequent visual measurements. Thus, improved calibration techniques are required to address lens distortion and out-of-focus blur in real-world settings. To this end, we propose the blur compensation weighted calibration (BCWC) framework, designed to enhance calibration accuracy under blur, constrained calibration distances, and non-ideal lens characteristics.

Recent advances in camera calibration have evolved along three primary directions: traditional geometric approaches, optimization-based machine learning, and self-calibration techniques. Traditional geometric methods rely on known calibration patterns and reprojection error analysis to estimate camera parameters accurately [12-15]. Meanwhile, optimization-based machine learning techniques have become increasingly prominent [16-17], employing advanced algorithms such as genetic algorithms [18], particle swarm optimization [19], and neural networks [20]. These techniques notably improve calibration accuracy and computational efficiency. Additionally, self-calibration methods, which rely solely on intrinsic camera data without external calibration patterns, have rapidly advanced [21-22]. Prominent examples include real-time stereo calibration [23], geometry-based closed-form solutions [24], and methods employing deep reinforcement learning [25]. Together, these developments underscore significant progress toward enhancing precision and versatility in camera calibration across diverse computer vision applications. Despite these advances, the use of two-dimensional planar calibration targets remains the mainstream approach for industrial camera calibration, primarily due to its portability, simplicity, and broad applicability in practical settings.

Traditional planar-based calibration methods perform well in short-range vision systems. However, for long-range vision applications, such as robotic navigation and large-scale measurement, captured images often suffer from out-of-focus blur. Out-of-focus severely affects the accuracy of feature extraction, which in turn degrades the overall calibration performance. In addressing the challenges associated with feature point localization in out-of-focus images, several strategies have been developed that leverage either the inherent characteristics of imaging patterns or advanced image processing techniques. One approach focuses on utilizing the native properties of traditional calibration targets, such as checkerboards and circular patterns, to refine feature extraction despite blur. Recent methods, including the use of phase regression networks [26] and hybrid localization algorithms based on radial symmetry [27], have demonstrated improved localization accuracy by exploiting the point spread function (PSF) characteristics inherent in out-of-focus images. Another strategy employs deconvolution algorithms based on Gaussian PSF models to restore feature clarity. Techniques such as automatic PSF estimation combined with Richardson-Lucy deconvolution [28] and Bayesian joint deconvolution frameworks [29] have been shown to effectively enhance feature retrieval from blurred images, particularly by dynamically adapting to varying out-of-focus levels. Furthermore, the use of active targets has emerged as an effective solution for mitigating out-of-focus effects. Active targets, including sinusoidal and circular fringe patterns, provide structured signals that improve feature point extraction under out-of-focus conditions. Early studies applied phase-shifting techniques for feature retrieval [30] while more recent approaches have introduced coded phase maps and Fourier-based decoding methods to enhance calibration performance. It is important to note that all phase-shift-based techniques typically require the acquisition of multiple images at each camera pose, making the calibration process cumbersome and limiting their practical application in dynamic or large-scale environments. Although high in precision, phase-shift-based methods are limited by their cumbersome requirement for capturing multiple images at each pose.

To address these limitations, this paper proposes the BCWC framework, which compensates for both out-of-focus blur and complex lens distortion. It incorporates a weighting scheme for improved feature point localization and introduces an optimized radial distortion parameter estimation method. This enables accurate calibration without strict focusing or displacement constraints. Unlike traditional techniques, such as Tsai’s method, the BCWC framework offers greater usability and flexibility. A flowchart of the framework is shown in Fig. 2. Additionally, our method improves lenses with manufacturing defects, outperforming methods such as Zhang’s calibration when applied to out-of-focus or degraded speckle images. Overall, the main contributions of this paper are summarized as follows:

1. A novel BCWC framework that computes initial digital image correlation (DIC) displacement values and integrates a weighting parameter into Tsai’s model to address blur.
2. In out-of-focus regions, the control point matching rate achieved 100%, and accuracy improved by 10% compared to the original Tsai model.

3. Experimental results show that the BCWC framework reduces camera reprojection errors by 17.2% and 15.6% relative to traditional methods.

This paper is organized as follows: Section 2 reviews related work; Section 3 introduces the proposed BCWC framework; Section 4 describes the methodology and implementation; Section 5 presents the experimental setup and results; Section 6 concludes with a summary and future directions.

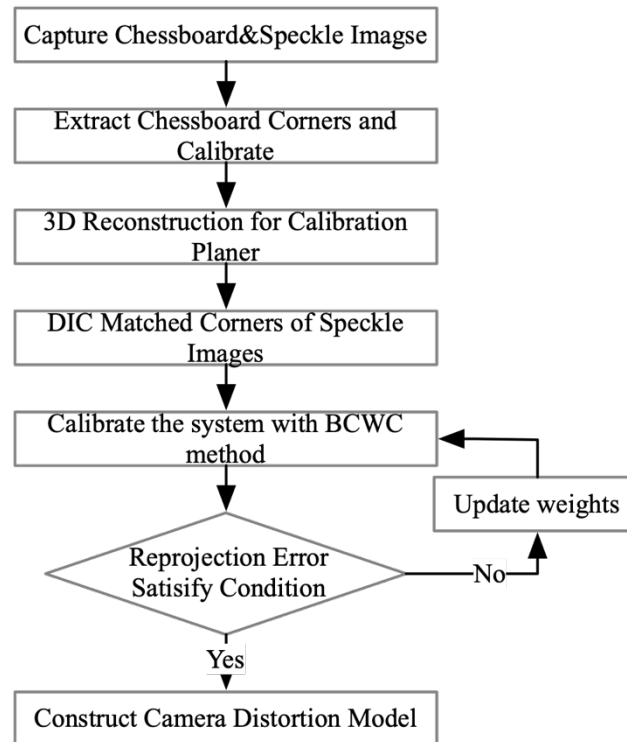


Fig. 2. Flow chart of the calibration framework

## 2 Related Works

This section provides a concise review of prior work on camera calibration algorithms, focusing on calibration point detection and the computation of camera parameters.

### 2.1 Calibration Point Detection

Accurate corner detection is critical for identifying key points that define the geometric relationship between three-dimensional (3D) real-world coordinates and two-dimensional (2D) image coordinates, directly influencing calibration accuracy.

For standard calibration patterns, such as chessboards and circular targets, traditional corner detection methods like Harris and SUSAN [31-32] are commonly used. These methods identify corners or circular mark centers based on grayscale value differences and subsequently refine coordinates to subpixel accuracy. However, these methods rely heavily on well-focused images, and their accuracy decreases notably when images are blurred or out of focus, particularly when using cameras with long focal lengths for close-range measurements.

To address the limitations associated with out-of-focus images, active calibration targets have been introduced, offering improved detection accuracy. Nevertheless, such methods often require multiple image acquisitions or color-coded patterns [33-35], increasing the operational complexity. Recently, computationally generated random speckle patterns have gained prominence due to their high contrast and robustness against out-of-focus and noise.

While blur affects the clarity and noise levels of individual speckle subsets, their morphological characteristics remain largely stable. The zero-mean normalized cross-correlation (ZNCC) criterion, commonly used in DIC, effectively mitigates lighting and noise variations, enabling precise subpixel-level matching between reference and target subsets.

Chen and Pan [36] utilized synthetic speckle patterns and DIC-based subset matching for camera and stereo calibration. However, their method’s performance declines under significant blur, affecting the reliability of SIFT-based feature matching. Yang [37] improved upon this by incorporating a perspective transformation as a shape function within DIC, allowing reliable initialization of control point positions under severe out-of-focus or scaling. Wu [38] further refined this approach by enhancing feature point detection accuracy, yielding improved initial estimations. However, Wu’s method still depends on Zhang’s calibration approach, which does not fully compensate for lens distortion stemming from manufacturing imperfections or misalignment.

In addition, deep learning-based corner detection techniques have recently shown considerable promise. Notably, DeTone’s SuperPoint [39] uses a self-supervised neural network to detect corners reliably and efficiently, but its performance degrades under challenging conditions.

## 2.2 Computation of Camera Parameters

Camera calibration algorithms generally fall into three primary categories: the direct linear calibration (DLC) method, Tsai’s method, and Zhang’s method.

The DLC method [40] is based on the pinhole camera model and estimates intrinsic and extrinsic parameters by solving a set of 3D–2D correspondences through direct linear transformation (DLT). Although it minimizes reprojection error via a linear approach, the method assumes an ideal lens free from distortion, which limits its applicability in realistic settings involving significant lens aberrations.

Tsai’s calibration method [41] adopts a two-step procedure: it first estimates extrinsic parameters from coplanar calibration points and subsequently refines intrinsic parameters and radial distortion coefficients via nonlinear optimization. While effective for predominantly radial distortions, this method exhibits limitations in the presence of tangential or asymmetrical distortions. Moreover, the initially computed rotation matrix may not satisfy orthogonality constraints, adversely affecting accuracy. To improve this, Zheng [42] incorporated an affine coordinate correction model, which enhances orthogonality and accuracy, albeit at the cost of increased computational complexity.

Zhang’s calibration method [10] offers improved flexibility by leveraging multiple planar images captured at various orientations. This enables the joint optimization of both intrinsic and extrinsic parameters through nonlinear procedures. Although effective under standard conditions, Zhang’s method may overlook asymmetrical distortions caused by lens misalignment, manufacturing defects, or focus variations, thereby reducing its robustness in practical applications.

To address these challenges, several advanced calibration techniques have been developed. Li [43] proposed a complex distortion field by segmenting radial distortion into multiple zones; however, the method involves high computational load due to the large number of unknowns. Ma [44] reduced this complexity by decreasing the number of parameters, though the model remained computationally intensive. Liu and Lu [45] introduced a more precise calibration method using non-coplanar feature points and weighted radial constraints. Their approach involved the computation of a bicubic spline surface to derive distortion coefficients, enabling a non-parametric model capable of capturing lens imperfections caused by manufacturing or assembly anomalies.

## 3 Blur Compensation Weighted Calibration Framework

This section introduces the BCWC framework, which is designed to mitigate the effects of out-of-focus blur and complex lens distortion in stereo vision systems. The framework consists of two principal components: a detection model for calibration points under out-of-focus conditions and a weighting model for compensating lens distortion.

### 3.1 Detection Model for Calibration Points Under Out-of-focus Condition

This component modifies the DIC calibration model using the Newton-Raphson optimization algorithm, as outlined in previous studies [45]. The original DIC calibration framework was introduced by Pan [36] in 2020, and

later enhanced by Yang [37], who refined the initialization of displacement vectors under defocused imaging conditions. This enhancement overcame prior limitations in applying DIC to scenarios involving significant blur.

For an arbitrary 2D point denoted as  $P_i = [u, v]^T$ , its corresponding 3D point in the world coordinate system is denoted as  $P_w = [X, Y, Z]^T$ . Let  $\tilde{P}_i$  represent the vector extended by adding 1 at the end:  $\tilde{P}_i = [u, v, 1]^T$  and  $\tilde{P}_w = [X, Y, Z, 1]^T$ . According to the pinhole camera model, the relationship between the 3D point  $P_w$  and its image projection  $P_i$  can be established as follows. The monocular pinhole-camera model is illustrated in Fig. 3.

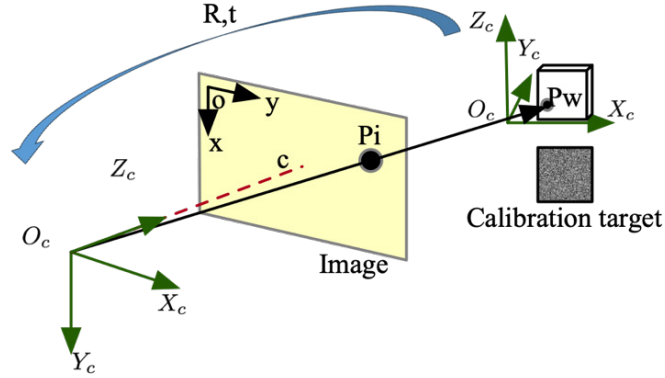


Fig. 3. The pinhole camera model

From the pinhole model, we derive equation (1):

$$s\tilde{P}_i = A[R \quad T]\tilde{P}_w. \quad (1)$$

$s$  is an arbitrary scaling factor,  $(R, T)$  are the extrinsic parameters, and  $A$  is the camera intrinsic matrix. In Zhang's [10] planar calibration model algorithm,  $Z$  is set to 0, so the equation can be simplified to:

$$s \begin{bmatrix} u \\ v \\ 1 \end{bmatrix} = [H]_{3 \times 3} \begin{bmatrix} X \\ Y \\ 1 \end{bmatrix}. \quad (2)$$

$H$  represents the homography matrix between two planes and considers capturing the same control point on the calibration target from two different viewpoints. The relationship between the two image points  $(u_1, v_1)$  and  $(u_2, v_2)$  can be expressed as follows:

$$s \begin{bmatrix} u_1 \\ v_1 \\ 1 \end{bmatrix} = H_1 H_2^{-1} \begin{bmatrix} u_2 \\ v_2 \\ 1 \end{bmatrix} = H_{12} \begin{bmatrix} u_2 \\ v_2 \\ 1 \end{bmatrix}. \quad (3)$$

As indicated by equation (3), image coordinates between two different perspectives can be transformed using the homography matrix. Therefore, in matching control points in speckle images captured from different perspectives based on DIC, the perspective transformation matrix can be used as the shape function instead of the homography matrix, as shown in equation (4).

$$W(x, y; p) = s \begin{bmatrix} x' \\ y' \\ 1 \end{bmatrix} = \begin{bmatrix} 1+u_x & u_y & u \\ v_x & 1+v_y & v \\ u_{xy} & v_{xy} & 1 \end{bmatrix} \begin{bmatrix} x \\ y \\ 1 \end{bmatrix}. \quad (4)$$

The coordinates  $(x, y)$  and  $(x', y')$  denote the positions in the reference and target subsets, respectively. The vector  $p = [u, u_x, u_y, u_{xy}, v, v_x, v_y, v_{xy}]^T$  represents the parameters of the perspective transformation. Compared to the commonly utilized ZNCC, the zero-mean normalized sum of squared differences (ZNSSD) offers superior performance in managing disturbances such as noise and lighting variations in images. As a result, this study adopts ZNSSD to evaluate the similarity between the reference and target subsets, as shown in equation (5), providing more stable, robust, and precise matching outcomes.

$$C_{\text{ZNSSD}}(\Delta p) = \sum_{x=-M}^M \sum_{y=-M}^M \left[ \frac{f(W(x, y; 0)) - \bar{f}}{\Delta f} - \frac{g(W(x, y; p + \Delta p)) - \bar{g}}{\Delta g} \right]^2. \quad (5)$$

Here,  $\Delta f = \sqrt{\sum_{x=-M}^M \sum_{y=-M}^M [f(x, y) - \bar{f}]^2}$  and  $\Delta g = \sqrt{\sum_{x=-M}^M \sum_{y=-M}^M [g(x', y') - \bar{g}]^2}$  normalize the intensity for the reference and target subsets, respectively.  $M$  represents the radius of the search subset. The functions  $f(x, y)$  and  $g(x', y')$  correspond to the grayscale intensities of the reference and target subsets. The incremental parameter  $\Delta p$  can be optimized iteratively using the Newton-Raphson minimization algorithm [45].

$$\Delta p = \left( (\nabla g J^T) (\nabla g J) \right)^{-1} \sum_{x=-M}^M \sum_{y=-M}^M \left\{ (\nabla g J^T) \left[ \frac{\Delta g}{\Delta f} (f - \bar{f}) - g(x, y; p) + \bar{g} \right] \right\}. \quad (6)$$

$J$  denotes the Jacobian matrix of the shape function  $W(x, y; p)$ , The expression for  $\frac{\partial W}{\partial p}$  is as equation (7).

$$\left\{ \begin{array}{l} J = \begin{bmatrix} \frac{1}{D} & \frac{x}{D} & \frac{y}{D} & -\frac{x \cdot U}{D^2} & 0 & 0 & 0 & -\frac{y \cdot U}{D^2} \\ 0 & 0 & 0 & -\frac{x \cdot V}{D^2} & \frac{1}{D} & \frac{x}{D} & \frac{y}{D} & -\frac{y \cdot V}{D^2} \end{bmatrix} \\ U = (1+u_x) \cdot x + u_y \cdot y + u \\ V = v_x \cdot x + (1+v_y) \cdot y + v \\ D = u_{xy} \cdot x + v_{xy} \cdot y + 1 \end{array} \right. \quad (7)$$

During the iterations,  $\nabla g = \left( \frac{\partial I}{\partial x}, \frac{\partial I}{\partial y} \right)$  represents the image gradient vector at the target subset in  $W(x; p)$ , as well as subpixel gray values of  $g(W(x', y'))$  can be calculated by Pan's method [46]. The deformation process of the target subset in the DIC matching algorithm is illustrated in Fig. 4. After calculating  $\Delta p$  using equation (6), the updated parameter vector  $p' = p + \Delta p$  can be computed. This process will repeat until convergence is achieved with high accuracy.

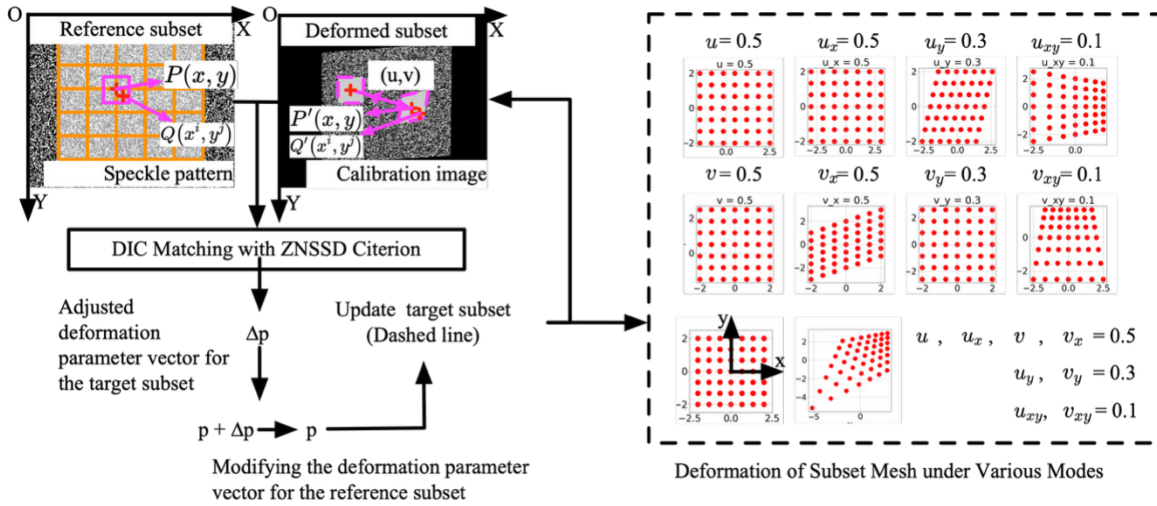


Fig. 4. Schematic principle of DIC matching

### 3.2 The Complex Lens Distortion Weighting Distribution Model

In this section, the classical Tsai distortion model is optimized based on the radial distortion parameter iterative model proposed by Liu [47]. The  $P'_d$ ,  $P_d$ ,  $P$  three points are assumed to represent the coordinates with distortion in the image coordinate system, the undistorted coordinates in the image coordinate system, and the coordinates in the world coordinate system. As illustrated in Fig. 5, the classical radial distortion model considers only radial distortion. Regardless of the distortion magnitude, the direction of the vector  $\overline{O_c P'_d}$  from the origin  $O_c$  on the image plane to the image point  $P'_d$  remains radially aligned with  $\overline{O_c P_d}$ , which extends from  $O_c$  to the point  $P_d$ ; they sharing the same direction with  $\overline{O_w P}$ .

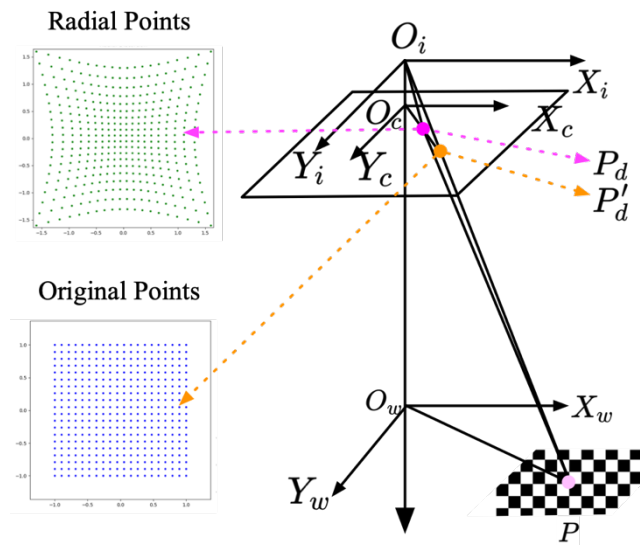


Fig. 5. Classical Tsai radial distortion model

Liu introduced several enhancements to the traditional Tsai model, which primarily addresses radial distortion. The pinhole camera model is presented in Fig. 2, with the camera's intrinsic matrix detailed in equation (8):

$$A = \begin{bmatrix} s_x \cdot f / d_x & \mathcal{G} & u_0 \\ 0 & f / d_y & v_0 \\ 0 & 0 & 1 \end{bmatrix}. \quad (8)$$

The focal length is denoted by  $f$ , while  $d_x$  and  $d_y$  represent the center-to-center distances of adjacent sensing elements in the  $X$  and  $Y$  directions, respectively. The skew coefficient of the camera optical axis is represented by  $\mathcal{G}$ , and  $(u_0, v_0)$  are the coordinates of the principal point in the computer image. The image scale factor,  $s_x$ , indicates the ratio of sampling intervals between the  $X$  and  $Y$  directions. For most digital image sensors, the pixel intervals  $d_x$  and  $d_y$  are identical, allowing the initial value of  $s_x$  to be set at 1. The external parameter matrix [R T], consisting of the rotation matrix  $R$  and the translation vector  $T$ , is described as follows:

$$R = \begin{bmatrix} r_1 & r_2 & r_3 \\ r_4 & r_5 & r_6 \\ r_7 & r_8 & r_9 \end{bmatrix}, T = \begin{bmatrix} T_x \\ T_y \\ T_z \end{bmatrix}. \quad (9)$$

The relationship between the actual image coordinates  $(X_d, Y_d)$  and the computer image coordinates  $(u, v)$  is delineated by equation (10).

$$\begin{cases} u = s_x d_x^{-1} X_d + \mathcal{G} Y_d + u_0 \\ v = d_y^{-1} Y_d + v_0 \end{cases}. \quad (10)$$

Here,  $(X_d, Y_d)$  represents the undistorted computer image coordinates of any point  $P$ , and  $(X'_d, Y'_d)$  denotes corresponding distorted computer image coordinates. The relationship between the real and ideal image coordinates is expressed as described in equation (11):

$$\begin{aligned} X_d &= X'_d + \delta_x(X'_d, Y'_d) \\ Y_d &= Y'_d + \delta_y(X'_d, Y'_d) \end{aligned}. \quad (11)$$

The distortion variables for point  $P$  along the  $X$  and  $Y$  directions are denoted by  $\delta_x(X'_d, Y'_d)$  and  $\delta_y(X'_d, Y'_d)$ , respectively. Liu [47] use a bicubic spline surface reconstruction method [48] to develop a weighted imaging plane distortion model by constructing the reprojection error of calibration feature points. During the calibration process, an iterative weighted radial alignment constraint method is utilized to improve calibration accuracy; the reprojection error serves as the criterion for ceasing the iteration. The distortion in  $x$ -direction for any point  $Q$  represented as  $\delta_x(X_d, Y_d)$  can be calculated using equation (12), and the  $\delta_y(X_d, Y_d)$  in  $y$ -direction can be computed using a similar method.

$$V_x = \begin{bmatrix} V_x^{(i-1, j-1)} & V_x^{(i-1, j+0)} & V_x^{(i-1, j+1)} & V_x^{(i-1, j+2)} \\ V_x^{(i+0, j-1)} & V_x^{(i+0, j+0)} & V_x^{(i+0, j+1)} & V_x^{(i+0, j+2)} \\ V_x^{(i+1, j-1)} & V_x^{(i+1, j+0)} & V_x^{(i+1, j+1)} & V_x^{(i+1, j+2)} \\ V_x^{(i+2, j-1)} & V_x^{(i+2, j+0)} & V_x^{(i+2, j+1)} & V_x^{(i+2, j+2)} \end{bmatrix}$$

$$\delta_x(X_d, Y_d) = \frac{1}{36} \begin{bmatrix} X_d^3 \\ X_d^2 \\ X_d^1 \\ X_d^0 \end{bmatrix}^T \cdot \begin{bmatrix} -1 & 3 & -3 & 1 \\ 3 & -6 & 3 & 0 \\ -3 & 0 & 3 & 0 \\ 1 & 4 & 1 & 0 \end{bmatrix} \cdot V_x \cdot \begin{bmatrix} -1 & 3 & -3 & 1 \\ 3 & -6 & 3 & 0 \\ -3 & 0 & 3 & 0 \\ 1 & 4 & 1 & 0 \end{bmatrix}^T \cdot \begin{bmatrix} Y_d^3 \\ Y_d^2 \\ Y_d^1 \\ Y_d^0 \end{bmatrix}. \quad (12)$$

## 4 Method

### 4.1 Overview

This section presents a three-step calibration framework for the BCWC method. First, calibration points are identified on the target image through DIC matching using a reference image. Second, intrinsic and extrinsic parameters of the stereo vision system are estimated using initial values obtained from Zhang's calibration method. BCWC refinement is then performed by applying radial constraints with weighted parameters. Finally, both internal and external camera parameters are optimized by minimizing the reprojection error associated with the identified calibration points.

This framework incorporates a modified DIC calibration model based on the Newton-Raphson optimization algorithm [45]. The DIC algorithm was initially proposed by Pan [36] in 2020 and later enhanced by Yang [37], who improved the initialization of displacement vectors under defocused conditions, thereby addressing limitations in prior applications.

### 4.2 DIC Matching Before Calibration Points

A simulated random speckle pattern serves as the reference image, while speckle images captured by the camera are used as target images. This setup facilitates precise matching between control points in the reference image and corresponding points in the target image. Due to the arbitrary placement of the calibration target plane within the camera's field of view, differences in pixel and transformation scales often arise between reference and target images. Although the relationship between these images is described by a perspective transformation shape function (equation (4)), accurate estimation of the initial values  $p$  is essential to ensure the convergence of the iterative process.

To match control points in the reference image with those in the transformed target image, the speckle pattern in the target image is adjusted to emulate the pixel scale of the reference. This allows for coarse matching via a fixed subset search, as described in [49]. The transformation between the reference and target images is modeled as a perspective transformation, enabling the calculation of the deformation function  $W$ , which is used to transform control points and extract the displacement vector  $p$  as the initial deformation estimate of the target subset.

To align the control points in the reference image with their counterparts in the transformed target image, the speckle pattern in the target image is converted into a new pattern that mimics the pixel scale of the reference image. This conversion allows for coarse matching through a fixed subset search. Given that the transformation relationship between the reference and target images is typically a perspective transformation, the deformation function  $W$  can then be obtained. This function transforms the control points between the reference and target images, extracting the displacement vector  $p$  as the initial value for the deformation of the target subset.

Fig. 6 illustrates the entire process of calculating the deformation function :

#### 1. Median Filtering:

The calibration image undergoes median filtering [50], followed by conversion to a binary image [45]. In this process, pixel values above a predefined threshold are set to 255, while those below are assigned a value of 0, as shown in Fig. 6(b).

#### 2. Edge Detection:

Morphological operations, including closing and opening with suitable structural elements, are applied to the binary image. These steps are followed by edge detection [51] to accurately delineate the contours of the speckle patterns, as shown in Fig. 6(c).

#### 3. Computation of Perspective Transformation Matrix:

A perspective transformation matrix is calculated using four pairs of corresponding vertices identified in the reference and target images. Once the initial displacement vector is established, a search radius is defined, and matching is performed within a square window around each control point in the target image using a fixed window search approach.

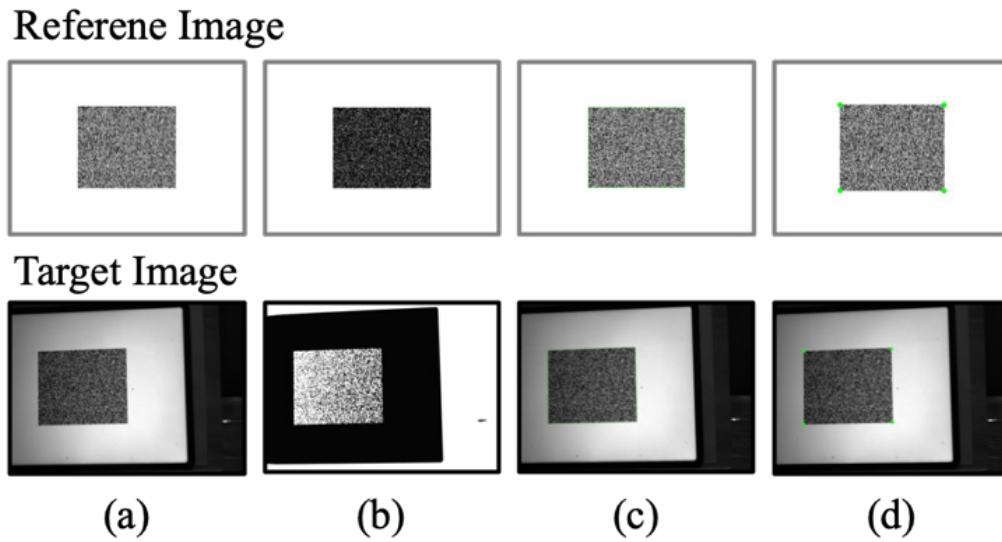


Fig. 6. Process of corner detection in speckle images

### 4.3 Calibrating Intrinsic and Extrinsic Parameters

As illustrated in Fig. 7, the stereo vision system consists of two cameras equipped with separate lenses. The calibration procedure is performed using a grid target consisting of 9 horizontal and 11 vertical lines. The intersections of these lines form corner points with known, fixed spatial distances, enabling precise geometric reference during calibration.

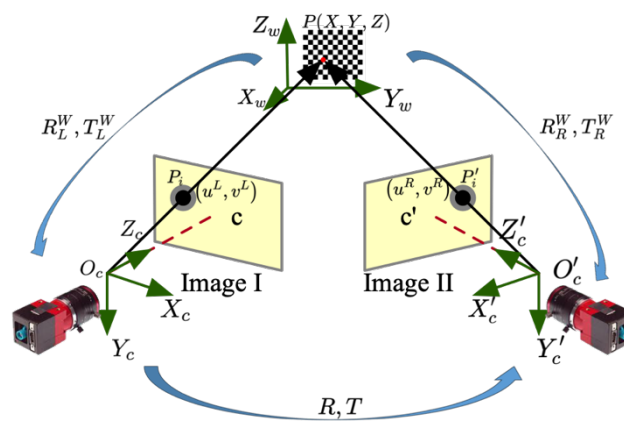


Fig. 7. Diagram of the stereoscopic vision calibration process

For any calibration point  $P$  on the chessboard grid in the world coordinate system  $O_w X_w Y_w Z_w$ , the relationships between its 3D reconstruction coordinates  $(X, Y, Z)$  and the left image coordinates  $(u^L, v^L)$ , as well as between  $(X,$

$Y, Z$ ) and the right image coordinates  $(u^R, v^R)$ , are described as follow:

$$\begin{aligned} z_L \begin{bmatrix} u^L \\ v^L \\ 1 \end{bmatrix} &= K_L [R_L^W, T_L^W] \begin{bmatrix} X \\ Y \\ Z \\ 1 \end{bmatrix} \\ z_R \begin{bmatrix} u^R \\ v^R \\ 1 \end{bmatrix} &= K_R [R_R^W, T_R^W] \begin{bmatrix} X \\ Y \\ Z \\ 1 \end{bmatrix}. \end{aligned} \quad (13)$$

Here,  $R_L^W$  and  $T_L^W$  denote the rotation and translation matrices that represent the transformation from the left image coordinate system to the world coordinate system. Similarly,  $R_R^W$  and  $T_R^W$  are the rotation and translation matrices, respectively, representing the transformation from the right image coordinate system to the world coordinate system. The intrinsic matrices of the left and right cameras are represented by  $K_L$  and  $K_R$  respectively.  $z_L$  and  $z_R$  represent the scaling factors. Upon extracting the corner image coordinates from the chessboard image, the intrinsic matrices  $K_L, K_R$  and the external parameters  $R_L^W, T_L^W, R_R^W, T_R^W$  of both cameras can be calculated using the Zhang calibration method [10]. These parameters facilitate stereo matching and the reconstruction of the 3D coordinates of the calibration board using epipolar geometry.

#### 4.4 Optimizing Camera Parameters with Weighted Radial Constraints

Due to the inherent design of lenses, distortion is minimal near the imaging center and increases with radial distance. Consequently, feature points located closer to the image center more accurately reflect the true correspondence between image coordinates and object space coordinates. In contrast, feature points near the image periphery are subject to more pronounced distortion, reducing the accuracy of the calibration model.

To improve overall calibration accuracy, it is beneficial to introduce a weighting scheme inversely proportional to the distance from the lens center. This approach allows the calibration process to emphasize centrally located feature points—where distortion is minimal—while still incorporating data from peripheral regions. Rather than excluding edge points entirely, the method balances their influence, resulting in more comprehensive data utilization and improved global calibration robustness.

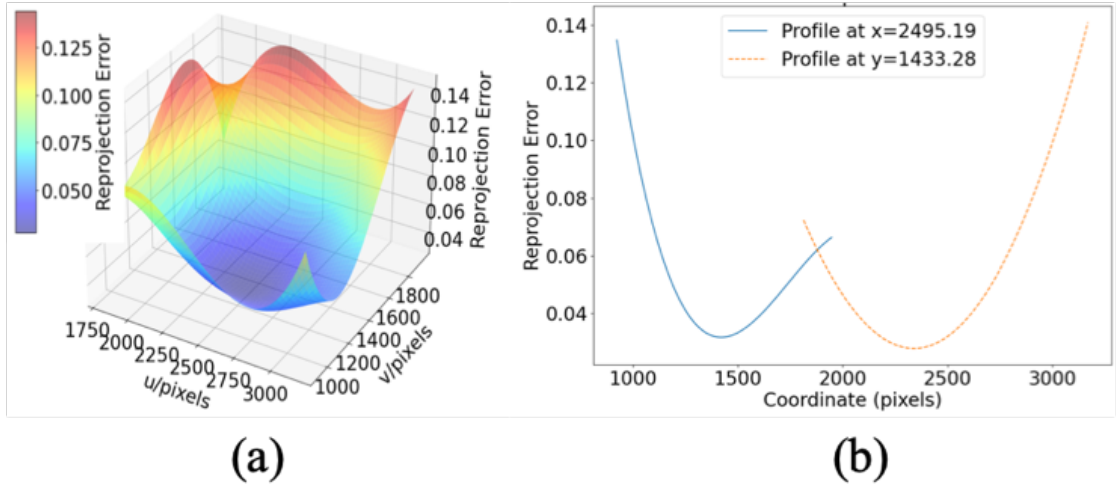
The weighting principle assigns larger weights to feature points with smaller reprojection errors. Ideally, the mean reprojection error should converge toward zero. Fig. 8(a) presents the reprojection error distribution surface for the left camera, along with cross-sectional profiles in the  $x$  ( $u$ ) and  $y$  ( $v$ ) directions. The weight distribution is quantified using a two-dimensional Gaussian function, as described by equation (14).

$$w_i(X_{di}, Y_{di}) = \frac{1}{2\pi\sigma_x\sigma_y} \exp\left(-\left(\frac{\Delta X_{di}^2}{2\sigma_x^2} + \frac{\Delta Y_{di}^2}{2\sigma_y^2}\right)\right). \quad (14)$$

Fig. 8(b) shows a Gaussian function to compute weights for each feature point, where  $\Delta X_{di}$  and  $\Delta Y_{di}$  represent the reprojection errors of the feature points in the image coordinate system, and  $\sigma_x$  and  $\sigma_y$  denote the standard deviations of these errors.

From equation (1), the relationship between any point in the 3D camera coordinate system  $(x, y, z)$  and its coordinates in the world coordinate system  $(X, Y, Z)$  is established as equation (15).

$$\begin{cases} x = r_1 X + r_2 Y + r_3 Z + T_x \\ y = r_4 X + r_5 Y + r_6 Z + T_y \\ z = r_7 X + r_8 Y + r_9 Z + T_z \end{cases} \quad (15)$$



(a) The distortion magnitude in left imaging system (b) profile views at specific coordinates

**Fig. 8.** The distortion field of camera imaging system

Assuming no lens distortion, the ideal image coordinates  $(X_d, Y_d)$ , world coordinates  $(X, Y, Z)$  and camera calibration parameters satisfy the following equation:

$$\begin{cases} x = r_1 X + r_2 Y + r_3 Z + T_x \\ y = r_4 X + r_5 Y + r_6 Z + T_y \\ z = r_7 X + r_8 Y + r_9 Z + T_z \end{cases} \quad (16)$$

In this experiment, the position of the calibration planer within the world coordinate system was determined using a stereo imaging system, thereby considering the value of the Z-axis in the world coordinate system. The camera calibration process for radial distortion incorporating weighting can be illustrated in pseudocode 1:

---

**Algorithm 1.** Weight radial calibration method

---

Input: Captured\_Images\_Left&Right, DIC\_Matched\_Points\_Left&Right  
 Output: Optimized Calibration Parameters

- 1: for j from 1 to Images\_Counts do:
- 2:  $K_L, K_R, R_{Lj}, T_{Lj}, R_{Rj}, T_{Rj} \leftarrow$  Calibrate stereo with DIC matched points
- 3:  $(X_{dj}, Y_{dj}) \leftarrow$  Compute image coordinates with  $(d_x, d_y)$
- 4:  $P_{world}(X_j, Y_j, Z_j), P_{camera}(x_j, y_j, z_j) \leftarrow$  Compute disparity map
- 5: for camera in Stereo do :
- 6: for i from 1 to Corner\_Counts do :
- 7: Construct  $\Gamma_{ji}$  and  $\alpha_j$
- 8:  $\alpha_j \leftarrow$  Solve  $\Gamma_{ji} \alpha_j^T = X_{dji}$
- 9: Construct  $\Psi_{ji}$  and  $\beta_j$
- 10:  $\beta_j \leftarrow$  Solve  $\Psi_{ji} \beta_j^T = Y_{dji} \cdot (Z_{ji} - T_{Lj2})$
- 11: end for
- 12: end for
- 13: end for

---

After using Zhang's method calibrate stereo cameras, the initial values of camera intrinsic parameters  $K_L, K_R$  and extrinsic parameters for each image pair  $R_{Lj}, T_{Lj}, R_{Rj}, T_{Rj}$  can be computed. The calibration planer can then be reconstructed in 3D.

If  $\vartheta$  in equation (8) is assumed to be zero, through transformation equation (16), the relationship between the world coordinates  $(X, Y, Z)$  and the image coordinates  $(X_d, Y_d)$  can be established.

$$\begin{aligned} \Gamma_{ji} &= [Y_{dji}X_{wi}, Y_{dji}Y_{wi}, Y_{dji}Z_{wi}, Y_{dji}, -X_{dji}X_{wi}, -X_{dji}Y_{wi}, -X_{dji}Z_{wi}] \\ \alpha_j &= [s_x r_1 / T_y, s_x r_2 / T_y, s_x r_3 / T_y, s_x T_x / T_y, r_4 / T_y, r_5 / T_y, r_6 / T_y] \end{aligned} \quad (17)$$

For each feature point,  $\Gamma_{ji}$  in equation (17) represents a known quantity, and the total number of feature points significantly exceeds the number of unknown parameters. Considering the varying weights of feature points, a weighted minimization function with equation (14) that compares actual coordinates  $X_{dj}$  with reprojection coordinates  $\Gamma_{ji}\alpha_j^T$  can be constructed as described in equation (18):

$$\begin{aligned} \Phi(\alpha_j) &= \sum_{i=1}^N w_{ji} (X_{dji} - \Gamma_{ji}\alpha_j^T)^2 = (X_{dj} - \Gamma_j\alpha_j^T)^T w_j (X_{dj} - \Gamma_j\alpha_j^T) \\ \alpha_j &= (\Gamma_j^T w_j \Gamma_j)^{-1} \Gamma_j^T w_j X_{dj} \end{aligned} \quad (18)$$

The subscript  $j$  denotes the index of each image pair. Setting  $\frac{d\Phi(\alpha_j)}{d\alpha_j}$  equal to 0 allows for the solution of the set of parameters  $\alpha_j$  using the following equation in pseudocode 2 :

---

**Algorithm 2.** Solution of camera extrinsic parameters

---

Input:  $\Gamma_{ji}, \alpha$   
Output: Rotation matrix  $R, T_x, T_y$

- 1:  $|T_y| \leftarrow (a_5^2 + a_6^2 + a_7^2)^{-1/2}$
- 2:  $s_x \leftarrow (a_1^2 + a_2^2 + a_3^2)^{-1/2} |T_y|$
- 3: if  $|T_y| = +|T_y|$  then :
- 4:  $r_1 = \alpha_1 T_y / s_x,$   
 $r_2 = \alpha_2 T_y / s_x,$   
 $r_3 = \alpha_3 T_y / s_x,$   
 $T_x = \alpha_4 T_y,$   
 $r_4 = \alpha_5 T_y,$   
 $r_5 = \alpha_6 T_y,$   
 $r_6 = \alpha_7 T_y$
- 5: else :
- 6:  $T_y = -|T_y|$
- 7: end if

---

Similarly, equations can be formulated for the camera parameters  $f$  and vector  $T_z$  with feature points:

$$\begin{aligned} \Psi_{ji} &= [r_4 X_{ji} + r_5 Y_{ji} + r_6 Z_{ji} + T_{Lj2}, -d_y (v_i - v_0)] \\ \beta &= [f, T_z] \\ Y_{vj} &= Y_{dji} \cdot (Z_{ji} - T_{Lj2}) \end{aligned} \quad (19)$$

Similar to the solution used to equation (18), the set of parameters  $\beta_j$  can be solved in equation (19):

$$\begin{aligned} J(\beta_j) &= \sum_{i=1}^N w_{ji} (Y_{\psi_{ji}} - \Psi_{ji} \beta_j^T)^2 = (Y_{\psi_j} - \Psi_j \beta_j^T)^T w_j (Y_{\psi_j} - \Psi_j \beta_j^T) \\ \beta_j &= (\Psi_j^T w_j \Psi_j)^{-1} \Psi_j^T w_j Y_{\psi_j} \end{aligned} \quad (20)$$

After computing  $\alpha_j$  and  $\beta_j$ , the skew coefficient  $\mathcal{G}$  can be calculated from equation (9) and equation (16):

$$\mathcal{G} = \frac{1}{d_y (v - v_0)} \left[ (u - u_0) - \frac{s_x f x}{d_x z} \right]. \quad (21)$$

Thus, the camera's intrinsic parameters  $f$  and extrinsic parameters  $R$ ,  $T$  can be derived. According to the traditional Tsai two-step method [41], it is assumed that the center of the computer memory image frame coincides with the principal point of the camera. This is defined as the intersection of the lens optical axis with the imaging plane. However, in practice, due to lens manufacturing and assembly inaccuracies, the principal point often does not align with the center of the image sensor. Consequently, Liu implemented the DLT [40] algorithm, using a zoom technique to accurately locate the principal point. To circumvent the need for additional equipment, this study uses the principal point coordinates  $u_0$ ,  $v_0$  determined from the camera's intrinsic matrix calibrated in Section 4.3 as the initial values. By applying weighted parameters and minimizing the distance from all camera point coordinates to the principal point using equation (10), equation (16), and equation (21),  $u_0$ ,  $v_0$  can be optimized:

$$\begin{aligned} H(v_0) &= \sum_{i=1}^N w_{ji} \left( v_0 + \frac{f_j y_j}{d_y z_j} - v'_{ji} \right)^2 \\ \Pi(u_0) &= \sum_{i=1}^N w_{ji} \left( u_0 + \frac{s_x f_j x_j}{d_x z_j} + \frac{\mathcal{G} f_j y_j}{z_j} - u'_{ji} \right)^2 \end{aligned} \quad (22)$$

All internal and external parameters of the camera model have been previously determined. Subsequently, using the developed distortion model, the reprojection errors of the calibration points are calculated. The steps presented in Section 4.3 and Section 4.4 are repeated until the desired error range is achieved or the iterative adjustments are completed. The reprojection errors for all feature points in the camera can be calculated using equation (1), equation (10), and equation (11).

## 5 Experiments

### 5.1 Experimental Setup

As shown in Fig. 9, the stereo vision system consists of two cameras (1800U-1236m, Allied Vision), two lenses (FA2516A, Allied Vision), and a computer. Each camera has a resolution of  $4112 \times 3008$  pixels and a pixel size of  $3\mu m \times 3\mu m$ . The lenses are equipped with adjustable focal lengths. Image data are transmitted from the cameras to the computer via USB protocol. Both cameras are mounted on a beam-like bracket featuring a quick-release clasp, which is secured to an optical table for stability.

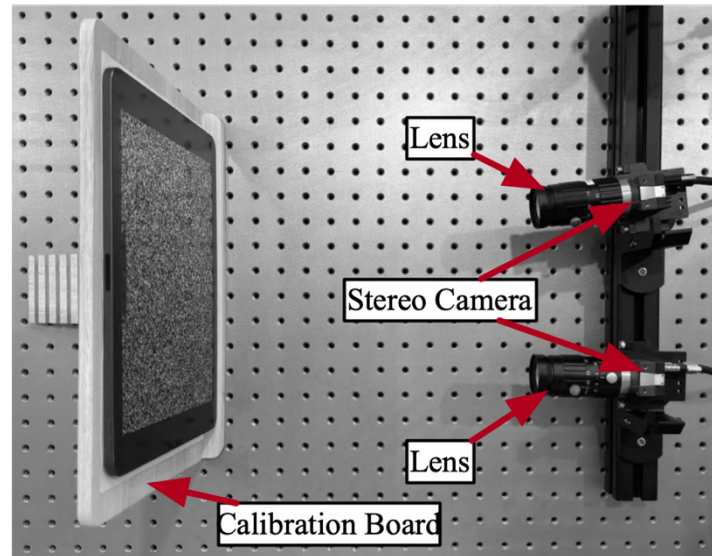


Fig. 9. The experimental setup of stereo camera system

In this experiment, a 12.9-inch iPad Pro is employed to display the speckle pattern. The iPad has a resolution of  $2732 \times 2048$  pixels and a physical pixel size of 0.09596 millimeters. The calibration target is a chessboard grid with 12 columns and 10 rows, resulting in a grid spacing of 100 pixels. This configuration yields a physical pattern size of approximately  $115.15\text{mm} \times 95.96\text{mm}$  and provides 63 calibration control points ( $9 \times 7$ ). A random speckle pattern is generated using the algorithm proposed by Zhou [52].

Fig. 10 illustrates the arrangement of corner points in the checkerboard calibration target. The spacing between adjacent corners is 9.5 mm. A discrete control point array is created on the simulated reference speckle image, analogous to the chessboard layout, facilitating accurate calibration through a predefined grid structure. The complete camera calibration workflow is presented in Fig. 11.

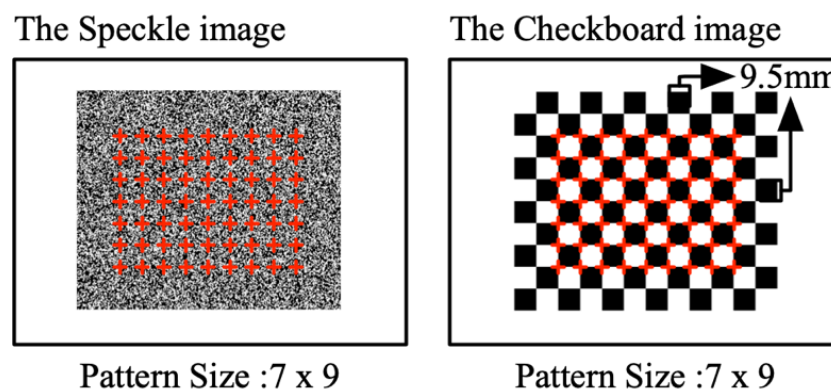


Fig. 10. Illustration of the checkerboard arrangement

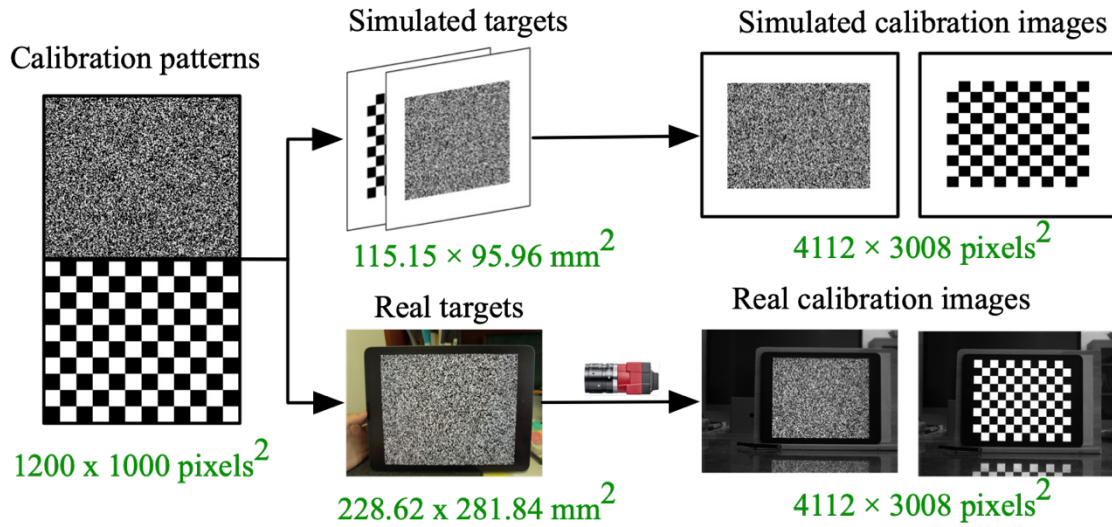


Fig. 11. Creation of calibration target and image capture for simulated and real-world tests

## 5.2 Relationship Between Image Blurriness and Calibration Accuracy of The BCWC Algorithm

**Comparison of Different Initial Displacement Method.** This subsection compares the performance of various feature point matching algorithms using random speckle patterns. Calibration targets were positioned at an approximate depth of 850 mm, and the speckle patterns were generated with parameters recommended by the Glare software [53]. The acquired images were subsequently processed in the OpenCorr [54] algorithm as target inputs.

Fig. 12 illustrates the feature point matching results. To test the stability of different algorithms, defocus blur was deliberately introduced by increasing the angle between the calibration plane and the optical axis of the camera. The comparison includes two initial estimation methods available in OpenCorr—scale-invariant feature transform (SIFT) and fast Fourier transform cross-correlation (FFTCC)—alongside the proposed method.

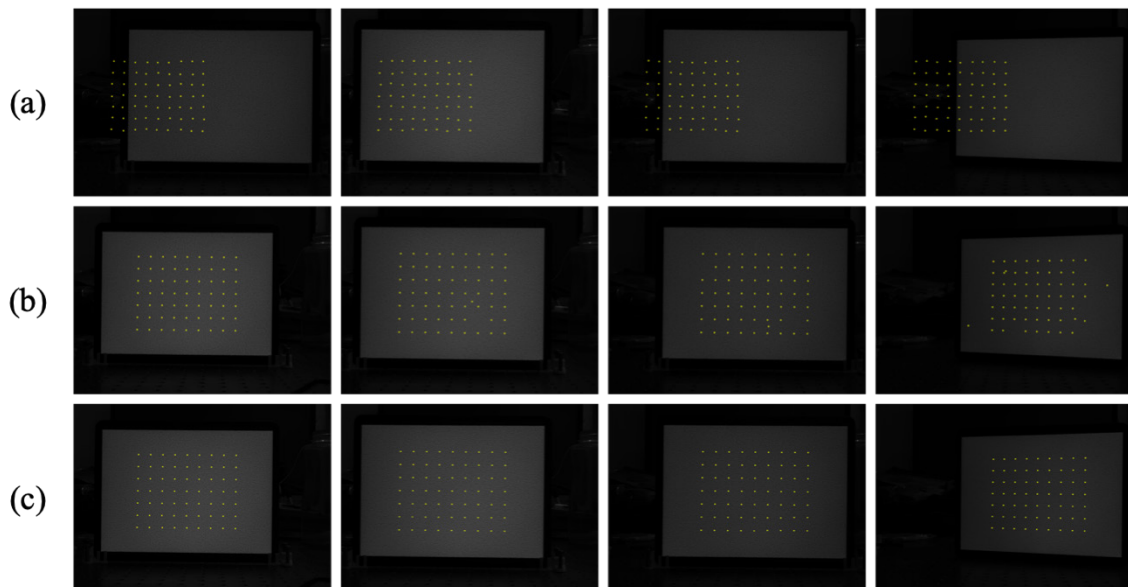


Fig. 12. DIC matched points visualization

FFTCC typically excels in scenarios involving small-scale deformations and minimal noise. However, under large-scale DIC changes caused by significant viewpoint variations and pronounced defocus blur, FFTCC experiences severe performance degradation. This deterioration primarily stems from its reliance on frequency domain correlation, where blurred or excessively transformed images result in weak and ambiguous correlation peaks. Consequently, this leads to substantial errors in displacement estimation, as evidenced by Table 1, where the maximum error frequently exceeded thousands of pixels.

Similarly, although SIFT demonstrates robustness against changes in scale, rotation, and illumination due to its gradient-based descriptors, it suffers notably under severe defocus conditions. The key reason for this performance drop is the diminished gradient information available in significantly blurred images. Under these conditions, SIFT descriptors become unstable and unreliable, resulting in considerable fluctuations in matching accuracy, with maximum errors occasionally surpassing 10,000 pixels, as shown in Table 1.

**Table 1.** Comparison of initial displacement estimation errors using different methods

Method	Mean error	Max error	Min error	Std dev
FFTCC	457.04	524.03	389.75	38.26
	433.19	568.40	300.78	77.83
	993.46	1124.53	859.45	78.68
	991.93	1125.63	855.01	79.62
	1549.89	2957.73	155.90	782.52
	1547.53	2955.26	110.84	783.28
	1395.03	2722.44	135.41	700.48
SIFT	5.77	16.18	0.82	3.29
	11.08	311.66	0.90	38.64
	79.12	4239.86	1.85	535.21
	30.78	907.65	0.78	138.43
	1271.61	10762.78	3.43	1288.16
	1173.26	1920.81	3.47	448.18
	1127.56	1882.72	4.21	454.01
Proposed	0.52	1.05	0.48	0.2
	0.77	1.19	0.29	0.32
	0.66	1.14	0.41	0.25
	0.59	1.11	0.27	0.34
	0.83	1.16	0.35	0.37
	0.71	1.02	0.63	0.16
	0.48	1.01	0.23	0.42

In contrast, the proposed method capitalizes on the inherent stability of speckle patterns' structural characteristics. By combining binarization, edge detection, and morphological processing, this method reliably identifies stable feature points within high-contrast regions. Unlike FFTCC, it does not solely depend on correlation peaks vulnerable to image blur, nor does it rely heavily on gradient descriptors susceptible to defocus like SIFT. Therefore, the proposed method consistently maintains high accuracy across various challenging imaging conditions. Experimental results demonstrate that this method achieves mean errors consistently below 1.19 pixels and maximum errors not exceeding 1.2 pixels. Furthermore, its standard deviations remain below 0.5 pixels across all datasets, clearly validating its superior robustness and reliability in large-scale DIC displacement estimations.

**Comparison of Optimization Algorithm.** To validate the performance of the proposed optimization algorithm on conventional cameras, additional experiments were conducted using an HBVCAM-W202011HD V33 camera. Calibration images were acquired at an approximate depth of 400 mm using a standard checkerboard as the calibration target. These images were then used as input for both the OpenCV calibration routine and the proposed method. The results are summarized in Table 2. Furthermore, the experiment evaluated the effectiveness of using OpenCV-derived parameters as initial values for subsequent optimization.

**Table 2.** Internal parameters of different method

Camera	Zhang's method	Proposed method	Proposed method without initial guess
$f_x$ / px	671.98	669.72	669.73
$f_y$ / px	670.24	668.34	669.71
$u_0$ / px	607.17	606.95	606.75
$v_0$ / px	380.41	380.41	380.41
Reprojection error/px:	0.649	0.587	0.628

From Table 2, it is evident that the proposed method yields more accurate calibration results compared to the standard Zhang's method. Specifically, the reprojection error was reduced from 0.649 pixels to 0.587 pixels when using the proposed algorithm with Zhang's output as the initial guess. Even without providing an initial estimate, the proposed method achieved a lower reprojection error of 0.628 pixels, demonstrating strong convergence capability and robustness.

While minor variations in intrinsic parameters—particularly in focal length and principal point coordinates—were observed, they indicate that the proposed method successfully refines the baseline calibration. However, the absence of reliable initial values leads to a slight decrease in accuracy. In such cases, more iterations are required, and convergence may reach a slightly suboptimal solution. Nevertheless, the method consistently outperforms Zhang's approach in terms of reprojection error, validating its effectiveness and reliability.

**Calibration Results Based on Camera Reprojection Error.** This subsection evaluates the calibration accuracy of the proposed BCWC algorithm. Initially, the calibration target (checkerboard) was placed at varying depths ranging from 800 mm to 1000 mm. As shown in Fig. 9, Fig. 10 stereo image pairs were captured from different viewpoints. The calibration results using Zhang's method are presented in Table 3, yielding a reprojection error of approximately 0.0147 pixels.

With the chessboard in sharp focus, stereo calibration was first performed using clear images and the OpenCV algorithm. To simulate defocus blur, Gaussian blur with a kernel size of 11 and a standard deviation of 3.6 was applied to the images. The calibration results are summarized in Table 3.

A comparison of the reprojection errors under in-focus and out-of-focus conditions shows that the error for Camera 1 rose from 0.01474 px to 0.02074 px, and for Camera 2 from 0.02059 px to 0.02466 px. This increase indicates that reduced image sharpness degrades the accuracy of feature point extraction, leading to less precise estimation of calibration parameters such as the intrinsic values ( $f_x, f_y$ ), principal point ( $u_0, v_0$ ), and distortion coefficients ( $k_1, k_2$ ).

**Table 3.** Internal parameters of Zhang's method

Camera	In-focus condition		Out-of-focus condition	
	Camera 1	Camera 2	Camera 1	Camera 2
$f_x$ / px	7397.7	7506.0	7402.9	7419.9
$f_y$ / px	7391.7	7504.3	7397.4	7409.6
$u_0$ / px	2092.444	2133.748	2084.142	2190.005
$v_0$ / px	1464.918	1465.920	1463.629	1467.017
$k_1$	-0.033	-0.000	-0.051	-0.021
$k_2$	0.976	-1.145	1.764	-0.113
Reprojection error/px:	0.01474	0.02059	0.02074	0.02466

Subsequently, the proposed BCWC algorithm was applied for calibration under out-of-focus conditions, following the procedure illustrated in Fig. 2. One of the calibration results using the BCWC distortion model is presented in Table 4.

**Table 4.** Calibration results of BCWC for two cameras

Calibration parameter	Camera 1	Camera 2
$f/mm$	22.2295	22.0916
$\theta$	0.0095	-0.0429
$s_x$	1.000	0.9999
$u_0$	2075.233	2161.2172
$v_0$	1469.559	1479.7669
Rotation matrix	$\begin{bmatrix} 0.9999 & -0.0102 & -0.0046 \\ 0.0104 & 0.9991 & 0.0402 \\ 0.0042 & -0.0403 & 0.9992 \end{bmatrix}$	$\begin{bmatrix} 0.9752 & -0.0049 & -0.2213 \\ 0.0138 & 0.9992 & 0.0385 \\ 0.2209 & -0.0406 & 0.9744 \end{bmatrix}$
Translation vector	$\begin{bmatrix} -97.4118 \\ -68.0633 \\ 953.8338 \end{bmatrix}$	$\begin{bmatrix} -97.4118 \\ -68.0633 \\ 953.8337 \end{bmatrix}$

Five different calibration methods were then applied to both defocused and well-focused image sets. In addition to the Tsai and Zhang methods, Liu's and Yang's methods were included for comparison under blurred conditions. The average reprojection errors for Liu and Yang's methods were 0.01759 pixels and 0.01726 pixels, respectively, while Zhang's method yielded an error of 0.01967 pixels. These average reprojection errors were computed by first calculating the reprojection error for each individual image, and then averaging over all collected images. Table 5 presents the reprojection errors across all methods, including the proposed BCWC approach.

**Table 5.** Reprojection errors of camera 1 under different conditions

Method	Reprojection error under in-focus condition	Reprojection error under out-of-focus condition	Mean error
Zhang's method	0.01874	0.02059	0.01967
Yang's method	0.01707	0.01745	0.01726
Tsai's method	0.01808	0.02047	0.01928
Liu's method	0.01696	0.01821	0.01759
Proposed method	0.01568	0.01685	0.01627

Experimental results indicate that the BCWC method consistently achieves the lowest reprojection error on the same set of calibration images. This performance advantage is attributed to multiple factors. Under out-of-focus conditions, the accuracy of corner localization decreases due to the instability of grayscale interpolation-based detection methods. In contrast, speckle patterns, owing to their high randomness, demonstrate greater robustness to blur, enabling more reliable feature extraction. Moreover, real-world lens distortion is rarely perfectly symmetrical. By introducing a weighting mechanism that assigns higher importance to features near the image center, the calibration process can better account for asymmetric distortion and improve parameter optimization. This targeted weighting strategy not only compensates for distortion irregularities but also enhances both the stability and accuracy of the calibration.

## 6 Conclusion

This paper proposed the Blur Compensation Weighted Calibration (BCWC) framework to address camera calibration challenges under out-of-focus imaging conditions and complex lens distortion. The method introduces two key innovations: a blur compensation strategy that enhances feature extraction robustness in defocused images, and a weighted radial constraint optimization that improves calibration accuracy by assigning higher significance to central image features. Unlike traditional calibration techniques, BCWC simplifies the calibration process and improves accuracy without requiring precise camera focusing or repetitive lens adjustments.

Experimental validation demonstrates significant improvements, achieving approximately 17.2% and 15.6% reductions in reprojection errors compared to Zhang's and Tsai's calibration methods, respectively.

Future research will focus on reducing computational complexity and extending the method to address other forms of image degradation, such as motion blur. Under extreme or rapidly changing lighting conditions, current solutions often rely on extended exposure or stabilization equipment, both of which have practical limitations. Overcoming these constraints will be essential for supporting broader real-world applications.

## References

- [1] D. Lee, S.-C. Kee, Efficient Camera–LiDAR Calibration Using Accumulated LiDAR Frames, *IEEE Access* 10(2022) 132349–132362.  
<https://doi.org/10.1109/ACCESS.2022.3230463>
- [2] K. Wang, C. Liu, S. Shen, Geometric Calibration for Cameras with Inconsistent Imaging Capabilities, *Sensors* 22(7) (2022) 2739.  
<https://doi.org/10.3390/s22072739>
- [3] Y. Liu, M. Liu, Y. Zhou, L. Dong, L. Kong, Camera calibration method based on improved DLT algorithm, in: *Proc. 2023 Optoelectronic Imaging and Multimedia Technology X*, 2023.  
<https://doi.org/10.1117/12.2686632>
- [4] E. Parrott, J.K. Pickard, R. Dubay, Practical Applications of a Set-Based Camera Deployment Methodology, *Sensors* 24(1)(2024) 111.  
<https://doi.org/10.3390/s24010111>
- [5] S. Fachada, D. Bonatto, A. Losfeld, G. Lafruit, M. Teratani, Pattern-free Plenoptic 2.0 Camera Calibration, in *Proc. 2022 IEEE 24th International Workshop on Multimedia Signal Processing (MMSP)*, 2022.  
<https://doi.org/10.1109/MMSP55362.2022.9949312>
- [6] S. Sobura, Calibration of Non-Metric UAV Camera Using Different Test Fields, *Geodesy and Cartography* 47(3)(2021) 111–117.  
<https://doi.org/10.3846/gac.2021.13080>
- [7] J. Huai, Y. Zhuang, Y. Lin, G. Jozkow, Q. Yuan, D. Chen, Continuous-time spatiotemporal calibration of a rolling shutter camera-IMU system, *IEEE Sensors Journal* 22(8)(2022) 7920–7930.  
<https://doi.org/10.1109/JSEN.2022.3152572>
- [8] Z. Dang, Y. Yuan, N. Geng, N.U.K. Khel, A Camera Calibration Method for Limited Motion of Target in Space, *Journal of Physics: Conference Series* 2560(1)(2023) 012014.  
<https://doi.org/10.1088/1742-6596/2560/1/012014>
- [9] K. Chaika, A. Filatov, A. Filatov, K. Krinkin, Automatic Wheels and Camera Calibration for Monocular and Differential Mobile Robots, *Applied Sciences* 11(13)(2021) 5806.  
<https://doi.org/10.3390/app11135806>
- [10] Z. Zhang, A flexible new technique for camera calibration, *IEEE Transactions on Pattern Analysis and Machine Intelligence* 22(11)(2000) 1330–1334.  
<https://doi.org/10.1109/34.888718>
- [11] D. Lee, Y.J. Oh, I.-K. Lee, Future-Frame Prediction for Fast-Moving Objects with Motion Blur, *Sensors* 20(16)(2020) 4394.  
<https://doi.org/10.3390/s20164394>
- [12] F. Barone, M. Marrazzo, C.J. Otón, Camera Calibration with Weighted Direct Linear Transformation and Anisotropic Uncertainties of Image Control Points, *Sensors* 20(4)(2020) 1175.  
<https://doi.org/10.3390/s20041175>
- [13] X. Liu, J. Tian, H. Kuang, X. Ma, A Stereo Calibration Method of Multi-Camera Based on Circular Calibration Board, *Electronics* 11(4)(2022) 627.  
<https://doi.org/10.3390/electronics11040627>
- [14] C. Ye, Z. Kang, X. Guo, A Camera-Lidar Calibration Method Assisted by Indoor Spatial Structure, *The International Archives of the Photogrammetry, Remote Sensing and Spatial Information Sciences XLVIII-1/W2-2023(2023)* 693–698.  
<https://doi.org/10.5194/isprs-archives-XLVIII-1-W2-2023-693-2023>
- [15] J.-Y. Kim, J.-E. Ha, Extrinsic Calibration of a Camera and a 2D LiDAR Using a Dummy Camera With IR Cut Filter Removed, *IEEE Access* 8(2020) 183071–183079.  
<https://doi.org/10.1109/ACCESS.2020.3029267>
- [16] J. Guo, Y. Zhu, J. Wang, S. Du, X. He, Research on camera calibration optimization method based on improved sparrow search algorithm, *Journal of Electronic Imaging* 32(1)(2023) 013040–013040.  
<https://doi.org/10.1117/1.JEI.32.1.013040>
- [17] Z. Lu, L. Cai, Camera calibration method with focus-related intrinsic parameters based on the thin-lens model, *Optics*

- Express 28(14)(2020) 20858–20878.  
<https://doi.org/10.1364/OE.392731>
- [18] L. Chen, F. Zhang, L. Sun, Research on the Calibration of Binocular Camera Based on BP Neural Network Optimized by Improved Genetic Simulated Annealing Algorithm, *IEEE Access* 8(2020) 103815–103832.  
<https://doi.org/10.1109/ACCESS.2020.2992652>
- [19] W. Fu, L. Wu, Camera calibration based on improved differential evolution particle swarm, *Measurement and Control* 56(1–2)(2023) 27–33.  
<https://doi.org/10.1177/00202940221101891>
- [20] K.-L. Zhang, H. Li, D. Ju, X. Wang, C. Guan, H. Fan, Optimization of tilt-shift lens camera calibration parameters based on genetic algorithm and artificial neural network, in: *Proc. 2024 Fourth International Conference on Image Processing and Intelligent Control (IPIC)*, 2024.  
<https://doi.org/10.1117/12.3038450>
- [21] S. Du, Y. Zhu, J. Wang, J. Yu, J. Guo, Underwater Camera Calibration Method Based on Improved Slime Mold Algorithm, *Sustainability* 14(10)(2022) 5752.  
<https://doi.org/10.3390/su14105752>
- [22] C. Dai, T. Han, Y. Luo, M. Wang, G. Cai, J. Su, Z. Gong, N. Liu, NMC3D: Non-Overlapping Multi-Camera Calibration Based on Sparse 3D Map, *Sensors* 24(16)(2024) 5228.  
<https://doi.org/10.3390/s24165228>
- [23] H. Yin, Z. Ma, M. Zhong, K. Wu, Y.-T. Wei, J. Guo, B. Huang, SLAM-Based Self-Calibration of a Binocular Stereo Vision Rig in Real-Time, *Sensors* 20(3)(2020) 621.  
<https://doi.org/10.3390/s20030621>
- [24] J.-H. Chuang, C.-H. Ho, A. Umam, H.-Y. Chen, J.-N. Hwang, T.-A. Chen, Geometry-Based Camera Calibration Using Closed-Form Solution of Principal Line, *IEEE Transactions on Image Processing* 30(2021) 2599–2610.  
<https://doi.org/10.1109/TIP.2020.3048684>
- [25] J. Ren, F. Guan, T. Wang, B. Qian, C. Luo, G. Cai, C. Kan, X. Li, High Precision Calibration Algorithm for Binocular Stereo Vision Camera using Deep Reinforcement Learning, *Computational Intelligence and Neuroscience* 2022(1) (2022) 1–10.  
<https://doi.org/10.1155/2022/6596868>
- [26] W. Hou, C. Zhou, H. Zhu, D. Zhang, Y. Wang, G. Jing, L. Liu, Phase-ReNet: a Phase regression network for feature detection from a defocused pattern for camera calibration, *Optica Open* 64(27)(2025) 7957–7967.  
<https://doi.org/10.1364/AO.564036>
- [27] X. Huang, Y. Ding, C. Xiao, W. Qian, C. Li, Hybrid algorithm based on radial symmetry and weighted least-square ellipse fitting for three-dimensional nanometer particle localization, *Journal of Biomedical Optics* 23(3)(2018) 036501.  
<https://doi.org/10.1117/1.JBO.23.3.036501>
- [28] G. Liu, S. Yousefi, Z. Zhi, R.K. Wang, Automatic estimation of point-spread-function for deconvoluting out-of-focus optical coherence tomographic images using information entropy-based approach, *Optics Express* 19(19)(2011) 18135–18148.  
<https://doi.org/10.1364/OE.19.018135>
- [29] N. Zhao, A. Basarab, D. Kouamé, J.-Y. Tourneret, Joint Bayesian deconvolution and pointspread function estimation for ultrasound imaging, in: *Proc. 2015 IEEE 12th International Symposium on Biomedical Imaging (ISBI)*, 2015.  
<https://doi.org/10.1109/ISBI.2015.7163857>
- [30] C. Schmalz, F. Forster, E. Angelopoulou, Camera calibration: active versus passive targets, *Optical Engineering* 50(11) (2011) 113601.  
<https://doi.org/10.1117/1.3643726>
- [31] C. Harris, M. Stephens, A Combined Corner and Edge Detector, in: *Proc. 1988 Alvey Vision Conference*, 1988.  
<https://doi.org/10.5244/C.2.23>
- [32] S.M. Smith, J.M. Brady, SUSAN—A New Approach to Low Level Image Processing, *International Journal of Computer Vision* 23(1)(1997) 45–78.  
<https://doi.org/10.1023/A:1007963824710>
- [33] T. Bell, J. Xu, S. Zhang, Method for out-of-focus camera calibration, *Applied Optics* 55(9)(2016) 2346–2352.  
<https://doi.org/10.1364/AO.55.002346>
- [34] H. Ha, Y. Bok, K. Joo, J. Jung, I.S. Kweon, Accurate camera calibration robust to defocus using a smartphone, in: *Proc. 2015 IEEE International Conference on Computer Vision (ICCV)*, 2015.  
<https://doi.org/10.1109/ICCV.2015.101>
- [35] Y. Wang, B. Cai, K. Wang, X. Chen, Out-of-focus color camera calibration with one normal-sized color-coded pattern, *Optics and Lasers in Engineering* 98(2017) 17–22.  
<https://doi.org/10.1016/j.optlaseng.2017.05.017>
- [36] B. Chen, B. Pan, Camera calibration using synthetic random speckle pattern and digital image correlation, *Optics and Lasers in Engineering* 126(2020) 105919.  
<https://doi.org/10.1016/j.optlaseng.2019.105919>
- [37] X. Yang, X. Chen, J. Xi, Perspective transformation based-initial value estimation for the speckle control points matching in an out-of-focus camera calibration using a synthetic speckle pattern, *Optics Express* 30(2)(2022) 2310–2325.

- <https://doi.org/10.1364/OE.448445>
- [38] J. Wu, M. Zhang, H. Wang, T. Shan, X. Zhang, R. Guo, A stable and effective calibration method for defocused cameras using synthetic speckle patterns, *Measurement Science and Technology* 34(8)(2023) 085011.  
<https://doi.org/10.1088/1361-6501/accd0d>
- [39] D. DeTone, T. Malisiewicz, A. Rabinovich, SuperPoint: Self-supervised interest point detection and description, in: *Proc. 2018 IEEE/CVF Conference on Computer Vision and Pattern Recognition Workshops (CVPRW)*, 2018.  
<https://doi.org/10.1109/CVPRW.2018.00060>
- [40] Y. I. Abdel-Aziz, H. M. Karara, M. Hauck, Direct Linear Transformation from Comparator Coordinates into Object Space Coordinates in Close-Range Photogrammetry, *Photogrammetric Engineering & Remote Sensing* 81(2)(2015) 103–107.  
<https://doi.org/10.14358/PERS.81.2.103>
- [41] R. Tsai, A versatile camera calibration technique for high-accuracy 3D machine vision metrology using off-the-shelf TV cameras and lenses, *IEEE Journal on Robotics and Automation* 3(4)(1987) 323–344.  
<https://doi.org/10.1109/JRA.1987.1087109>
- [42] H. Zheng, F. Duan, X. Fu, C. Liu, T. Li, M. Yan, A non-coplanar high-precision calibration method for cameras based on an affine coordinate correction model, *Measurement Science and Technology* 34(9)(2023) 095018.  
<https://doi.org/10.1088/1361-6501/acda51>
- [43] X. Li, W. Li, X. Yuan, X. Yin, X. Ma, DoF-Dependent and Equal-Partition Based Lens Distortion Modeling and Calibration Method for Close-Range Photogrammetry, *Sensors* 20(20)(2020) 5934.  
<https://doi.org/10.3390/s20205934>
- [44] X. Ma, P. Zhu, X. Li, X. Zheng, J. Zhou, X. Wang, K.W.S. Au, A minimal set of parameters-based depth-dependent distortion model and its calibration method for stereo vision systems, *IEEE Transactions on Instrumentation and Measurement* 73(2024) 1–11.  
<https://doi.org/10.1109/TIM.2024.3406802>
- [45] H. Lu, P.D. Cary, Deformation measurements by digital image correlation: Implementation of a second-order displacement gradient, *Experimental Mechanics* 40(4)(2000) 393–400.  
<https://doi.org/10.1007/BF02326485>
- [46] Z. Pan, W. Chen, Z. Jiang, L. Tang, Y. Liu, Z. Liu, Performance of global look-up table strategy in digital image correlation with cubic B-spline interpolation and bicubic interpolation, *Theoretical and Applied Mechanics Letters* 6(3)(2016) 126–130.  
<https://doi.org/10.1016/j.taml.2016.04.003>
- [47] X. Liu, R. Lu, Calibration of a stereo microscope based on non-coplanar feature points with iteratively weighted radial alignment constraint, *Optics and Lasers in Engineering* 127(2020) 105977.  
<https://doi.org/10.1016/j.optlaseng.2019.105977>
- [48] M. Eck, H. Hoppe, Automatic reconstruction of B-spline surfaces of arbitrary topological type, in: *Proc. 1996 Proceedings of the 23rd annual conference on Computer graphics and interactive techniques*, 1996.  
<https://doi.org/10.1145/237170.237271>
- [49] S. Baker, I. Matthews, Lucas-kanade 20 years on: A unifying framework, *International Journal of Computer Vision* 56(3)(2004) 221–255.  
<https://doi.org/10.1023/B:VISI.0000011205.11775.fd>
- [50] Z. Lv, F.-L. Wang, Y.-Q. Chang, Y. Liu, Region-adaptive median filter, *Journal of System Simulation* 19(23)(2007) 5411–5414.
- [51] J.F. Canny, Finding edges and lines in images, Technical Report, AITR-720, 1983.  
<http://hdl.handle.net/1721.1/6939>
- [52] P. Zhou, K.E. Goodson, Subpixel displacement and deformation gradient measurement using digital image/speckle correlation (DISC), *Optical Engineering* 40(8)(2001) 1613–1620.  
<https://doi.org/10.1117/1.1387992>
- [53] Y. Su, Q. Zhang, Glare: A free and open-source software for generation and assessment of digital speckle pattern, *Optics and Lasers in Engineering* 148(2022) 106766.  
<https://doi.org/10.1016/j.optlaseng.2021.106766>
- [54] Z. Jiang, OpenCorr: An open source library for research and development of digital image correlation, *Optics and Lasers in Engineering* 165(2023) 107566.  
<https://doi.org/10.1016/j.optlaseng.2023.107566>